PHYSICS

Suppressed terahertz dynamics of water confined in nanometer gaps

Hyosim Yang[1]†, Gangseon Ji[1]†, Min Choi[2], Seondo Park[3], Hyeonjun An[1], Hyoung-Taek Lee[1], Joonwoo Jeong[1], Yun Daniel Park[3], Kyungwan Kim[4], Noejung Park[1], Jeeyoon Jeong[5]*, Dai-Sik Kim[1,3]*, Hyeong-Ryeol Park[1]*

Nanoconfined waters exhibit low static permittivity mainly due to interfacial effects that span about one nanometer. The characteristic length scale may be much longer in the terahertz (THz) regime where long-range collective dynamics occur; however, the THz dynamics have been largely unexplored because of the lack of a robust platform. Here, we use metallic loop nanogaps to sharply enhance light-matter interactions and precisely measure real and imaginary THz refractive indices of nanoconfined water at gap widths ranging from 2 to 20 nanometers, spanning mostly interfacial waters all the way to quasi-bulk waters. We find that, in addition to the well-known interfacial effect, the confinement effect also contributes substantially to the decrease in the complex refractive indices of the nanoconfined water by cutting off low-energy vibrational modes, even at gap widths as large as 10 nanometers. Our findings provide valuable insights into the collective dynamics of water molecules which is crucial to understanding water-mediated processes.

INTRODUCTION

The behaviors of water molecules confined in nanoscale structures underlie various processes in our everyday life such as solvation of ions and biomolecules (*1*–*7*), molecular transport through nanopores (*8*, *9*), formation of electric double layer on electrodes (*10*, *11*), and chemical reactions (*12*, *13*). On this stance, understanding the properties of nanoconfined water is of paramount importance in all fields of natural science and has attracted many theoretical and experimental studies (*14*–*28*). Thus far, most studies have agreed on the rule of thumb that the nanoconfinement effect comes from the unique response of interfacial water, which forms an ordered state parallel to face of the interface up to 1-nm thickness (approximately four layers of water molecules), leading to a suppressed reorientation of molecular dipole moment under external field bias and consequently a decreased permittivity (*29*–*32*).

Decades of efforts have been paid to experimentally identify the permittivity of interfacial water in natural nanoporous materials (*8*, *19*, *33*). However, a direct systematic measurement of the permittivity of controlled nanoconfined waters was achieved only very recently (*34*). In this seminal work done in (*34*), a van der Waals assembly of two-dimensional (2D) materials was used to precisely control the thickness of water, and the permittivity is measured with an electrostatic force microscopy, which provides subpiconewton resolution to detect molecules with ultralow polarizabilities.

Static permittivity of nanoconfined water has been studied extensively in the past few years; however, similar progresses in its high-frequency counterpart have been lacking. Most optical measurements on nanoconfined water have been performed in systems whereby a sufficient surface area can be provided, such as with beryl crystals (*35*, *36*), silica aerosols (*8*, *37*), and metallic waveguides (*38*–*41*), yet without a reliable way to control the thickness of water below 10-nm regime. Thus far, the best way to control thickness of water at the nanometer scale is leak-controlled deposition of water vapor under ultrahigh vacuum and cryogenic temperatures (*42*, *43*). However, to be relevant to biological phenomena, where optical characterization and manipulation of biomolecules are becoming increasingly important, it would be ideal to have a platform where optical properties of nanowater can be systematically studied under ambient environment (*44*).

Optical nanoantennas are ideal for such purpose, as it can provide both nanoconfinement and an increased sensitivity at the same time. In particular, loop nanogap antennas support strong dipolar resonance and transmit light only through the gap without background transmission (*44*–*47*), allowing us to analyze light-matter interaction exclusively in the gap (*48*–*50*). Recently, it has also been demonstrated that liquid water can be filled into 10-nm-wide loop nanogaps by replacing a spacing dielectric layer with water molecules via etch-and-dilute process (*39*). Because the gap width is determined by thickness of the spacing dielectric layer (*44*, *51*), which can be nanometrically controlled in the deposition step, the loop nanogaps are ideal for systematic investigation of nanoconfined water at different thicknesses. In addition, the loop nanogap antenna, which can be fabricated on a wafer scale using atomic layer lithography, enables optical measurements of the vertically oriented nanometer-thick water layers in the long-wavelength regime to investigate long-range hydrogen bond networks, which could not be reached previously.

In this study, we optically measured water-filled rectangular loop nanogaps with gap widths of 2 to 20 nm to determine refractive indices of nanoconfined water at terahertz (THz) frequencies between 0.1 and 1.5 THz, from which one can access long-range collective dynamics responsible for solvation dynamics (*52*–*56*) (Fig. 1A). By way of the high sensitivity of loop nanogaps, together with the small spectral dispersion of water at THz frequencies, water-induced

[1]Department of Physics, Ulsan National Institute of Science and Technology, Ulsan 44919, Republic of Korea. [2]Department of Chemistry, Ulsan National Institute of Science and Technology, Ulsan 44919, Republic of Korea. [3]Department of Physics and Astronomy, Seoul National University, Seoul 08826, Republic of Korea. [4]Department of Physics, Chungbuk National University, Cheongju 28644, Republic of Korea. [5]Department of Physics and Institute for Quantum Convergence Technology, Kangwon National University, Chuncheon 24341, Republic of Korea.
†These authors contributed equally to this work.
*Corresponding author. Email: nano@unist.ac.kr (H.-R.P.); daisikkim@unist.ac.kr (D.-S.K.); peterjjy@kangwon.ac.kr (J.J.)

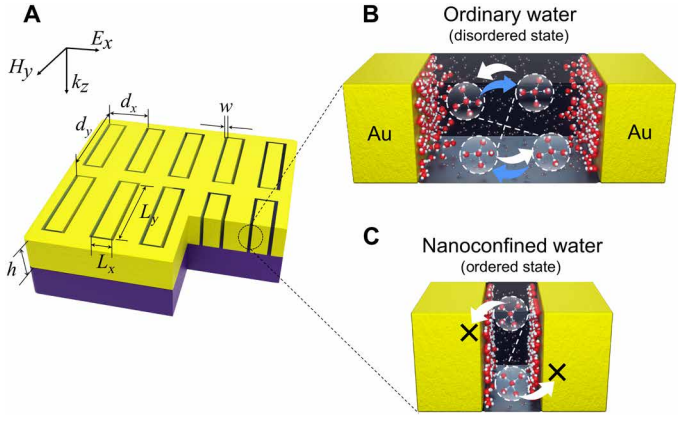

Fig. 1. Rectangular loop nanogaps filled with water. (**A**) Schematic diagram of a p-polarized THz electromagnetic wave incident on the confined water in metal nanogap loops for measuring long-range correlation of hydrogen bond networks depending on the gap width. The gap width w varies from 2 to 20 nm in different samples with the same metal thickness of $h = 200$ nm. Parameters of the nanogap loop array are as follows: L_x and L_y are the horizontal and vertical lengths of the rectangular loop, and d_x and d_y are the horizontal and vertical periods of the loop array. (**B** and **C**) The concepts of ordinary water and nanoconfined water are illustrated in (B) and (C), respectively.

changes in the resonant frequencies and amplitudes of the loop nanogaps could be unambiguously converted into complex refractive indices of the gap-filling nanoconfined water (*39*). The retrieved complex refractive indices of nanoconfined water were anomalously low compared to their bulk counterparts (Fig. 1B), being even lower at smaller gap widths (Fig. 1C). At the gap width of 2 nm, the real index was only 60% of the bulk value, and the imaginary index nearly approached zero. From complementary analyses, comprising ab initio calculation, coupled-mode calculation, effective medium theory, and vibrational density of states (VDOS) model, the suppressed Debye relaxation dynamics of quasi-bulk water at the center (Fig. 1C), which are not quite bulk-like despite being 10 nm away from the interface, explain the overall anomalously low complex refractive indices of the nanoconfined water at THz frequencies.

RESULTS

Preparation of nanoconfined water in metal gaps with various widths

Water-filled nanogap loops are realized in two steps; first, metal-insulator-metal gaps are fabricated using atomic layer lithography (*44*), and then the gap-filling insulator is substituted with liquid water using a wet-etch-and-dilution process (*39*). First, a 200-nm-thick gold layer with rectangular holes is patterned on a 500-μm-thick high-resistivity silicon wafer using conventional photolithography (Fig. 2A). In Fig. 2B, aluminum oxide is deposited conformally over the entire metallic pattern using atomic layer deposition (ALD) with an angstrom-scale precision. Aluminum oxide thickness varies from 2 to 20 nm. After the ALD process, a 200-nm-thick gold layer is secondly deposited to fill the rectangular hole, and the excess gold layer on top of the first metal pattern is exfoliated using an adhesive tape. Thus, vertically aligned nanogaps between the metals are formed, whose width is determined by the thickness of aluminum oxide deposited using ALD. The nanogap fabrication is completed by polishing the surface using Ar ion milling at an oblique angle (Fig. 2C). Next, to wet-etch the aluminum oxide on top of and inside the gap, nanogap samples are immersed in 1 M potassium hydroxide (KOH) solution for 1 to 10 min, depending on the gap width (Fig. 2D). Then, the samples are transferred to a deionized (DI) water bath ($R = 18.2$ megohm·cm) for dilution process. The wet-etch residues were completely replaced with water molecules after more than an hour (Fig. 2E). To prevent gap-filling water from vaporizing, a sapphire cover is attached to the sample with a 100-μm-thick double-sided Kapton tape as a spacer (Fig. 2F). The reservoir is further sealed on the sides with GE varnish during temperature-dependent measurements in a cryostat, preventing the gap water from leaking. It should be noted that the gap is always filled with aluminum oxide, KOH, or water, so that liquid water can be guaranteed to fill the gap after the whole process is completed. An empty gap is prepared as a reference by vaporizing the gap-filling water by critical point drying (CPD) (*57*). Detailed fabrication processes are shown in Materials and Methods. Cross-sectional scanning transmission electron microscopy (TEM) images and energy-dispersive spectroscopy (EDS) maps of Al_2O_3-filled and empty nanogaps (Fig. 2, G and H) suggest that the wet-etch process successfully removes aluminum oxide without damaging the gap, further confirming that our nanogaps are completely filled with water.

THz transmissions through empty and water-filled nanogaps

The nanogaps are characterized by THz time-domain spectroscopy (THz-TDS), as detailed in Materials and Methods. In Fig. 3A, the time-domain transmission signals of empty and water-filled nanogaps as well as their respective reference signals are presented (see the estimated THz near-field amplitudes at the gap in fig. S1 of the Supplementary Materials). It is evident from the time traces of narrower gaps that oscillation periods are longer than those of their 10-nm-gap counterparts, implying that resonances exist at lower frequencies due to stronger gap plasmon coupling at narrower gaps. Upon filling the gap with water, we observe a notable suppression of the tailing oscillation, which results from absorption introduced by the water filling the gap. In Fig. 3B, the corresponding frequency-domain transmission spectra are shown after Fourier-transforming the time traces in Fig. 3A. The introduction of water into the nanogap causes a red shift in all the resonant peaks of the samples and a decrease in peak amplitude. Noticeably, the decrease in amplitude is less pronounced in narrower gaps, which is counterintuitive because narrower gaps tend to exhibit larger spectral responses to changes in the dielectric environment near the gap. This is also evident from the blue dashed lines in Fig. 3B, which are analytically calculated spectra using the coupled-mode method with the refractive indices of bulk water (please refer to the details of coupled-mode method and THz complex refractive indices of bulk water in Supplementary Materials, figs. S3 and S4, respectively). These experimental results suggest that the gap-filling water can have a lower dielectric permittivity in THz region when the gap is narrower, similar to the earlier results in static and infrared regimes (*34*, *40*).

Estimation of THz complex refractive index of nanoconfined water

To quantitatively estimate refractive indices of the gap-filling water in THz region, we calculated transmission spectra of the nanogap sample (see the Supplementary Materials, fig. S5) and created 2D maps of the relative peak amplitudes and relative resonance frequencies as

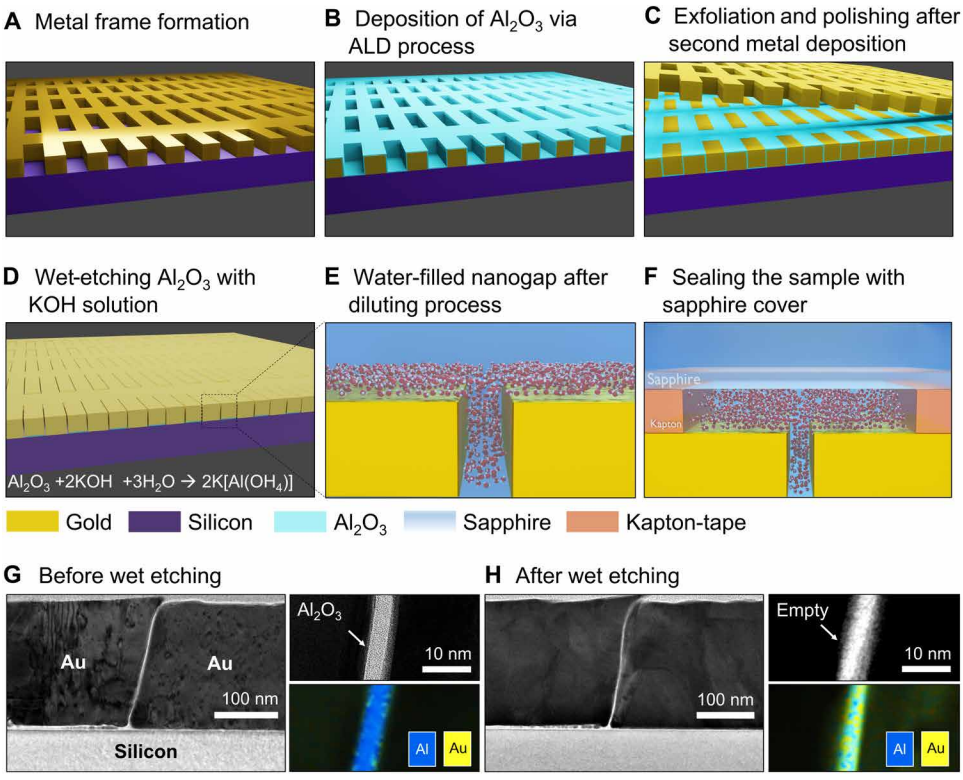

Fig. 2. Fabrication process of water-filled nanogap loops. (**A**) A gold frame patterned using conventional photolithography and lift-off process. (**B**) Atomic layer deposition of aluminum oxide at thicknesses ranging from 2 to 20 nm. (**C**) Exfoliation of excess metals following deposition of the second gold layer reveals planarized metal nanogaps with gap widths ranging from 2 to 20 nm. (**D**) By wet-etching the gap-filling aluminium oxide, the gap is filled with water and reaction intermediates. (**E**) By diluting the gap-filling solution using DI water, water-filled nanogaps can be achieved. (**F**) Water-filled nanogaps are sealed with a sapphire cover and a double-sided Kapton tape. (**G** and **H**) Cross-sectional scanning TEM images and EDS maps of the 5-nm gap (G) before and (H) after wet etching are shown.

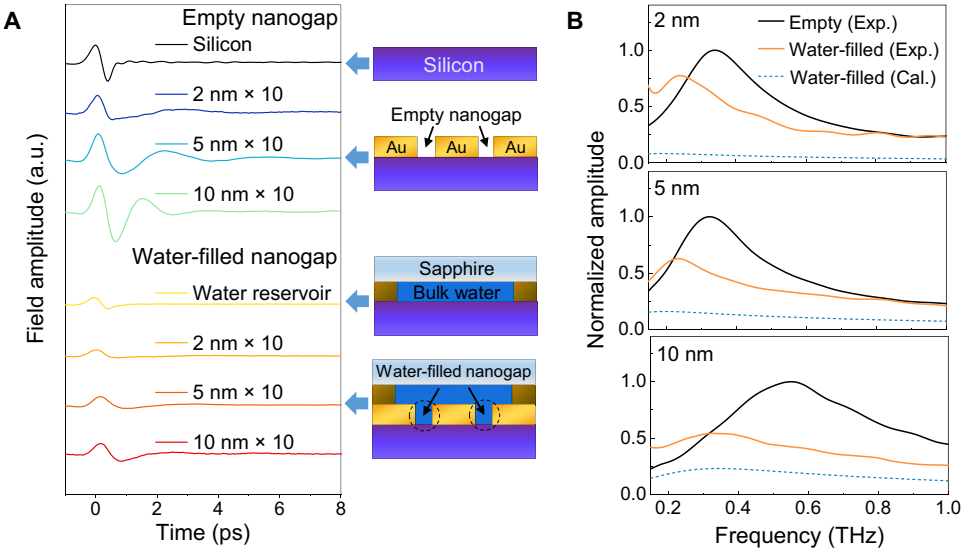

Fig. 3. THz transmissions of empty and water-filled nanogaps with different gap widths. (**A**) Time traces of THz pulses transmitted through nanogap samples with empty and water-filled gaps, as well as through a bare silicon substrate with and without a water reservoir. The time traces have been vertically offset for clarity. The time traces of 2-, 5-, and 10-nm gaps have been magnified 10 times to enhance visibility and highlight their small-scale fluctuations. As indicated by the arrows, each sample schematic is shown in the right panel of the graph. a.u., arbitrary units. (**B**) Normalized THz amplitude (transmitted electric field) spectra of empty (black solid) and water-filled (orange solid) nanogaps with the gap widths of 2, 5, and 10 nm, obtained by the THz-TDS. The blue dashed lines represent the normalized field spectra, calculated analytically by using the coupled-mode method assuming that the gap-filling water is bulk-like. In all cases, nanogap loop arrays contain the same parameters as follows: $L_x = 20$ μm, $L_y = 80$ μm, $d_x = 40$ μm, and $d_y = 100$ μm.

a function of complex refractive indices ($\tilde{n} = n + i\kappa$) of the gap-filling medium using the coupled-mode method, as shown in Fig. 4 (C and D). It should be noted that the relative peak amplitude and relative resonance frequency are normalized with respect to the values obtained from an empty gap. Because the resonance frequency is predominantly affected by the real part of the refractive index n, and the transmitted amplitude by the extinction coefficient κ (fig. S5), one can unanimously determine (n, κ) of the gap-filling water by analyzing the relative changes in peak amplitude and resonant frequency of the corresponding transmission spectrum. For example, a water-filled gap with a width (w) of 5 nm and a loop length [$L = 2(L_x + L_y)$] of 200 μm, as shown in Fig. 4 (A and B), exhibits a relative peak amplitude and resonance frequency of 63 and 73%, respectively, compared to an empty gap, representing a complex refractive index of $\tilde{n} = 1.5 + i\,0.082$ for the nanoconfined water at the resonance of the loop nanogap. Figure 4 (E and F) indicates a gradual decrease in the complex refractive indices of the residual water at thickness of around 10 nm and below. In the smallest gap at THz frequencies, the refractive index decreases by 40%, similar to the trend observed at infrared frequencies (*40*), while the extinction coefficient changes more markedly and reaches zero. It should be noted that in spite of the same loop length, the resonance peak in the spectrum varies when passing through a narrow gap of tens of nanometers or less, because of the gap plasmon effect (*46*). However, the observed phenomena are the result of confinement and are minimally affected by spectral dispersion; this is confirmed by an additional measurement at different resonant frequencies using smaller loop nanogaps with a loop length of $L = 100$ μm, while maintaining the same gap sizes at 5 and 20 nm (see the Supplementary Materials, fig. S6).

There is active debate as to why nanoconfined water has a low refractive index (*15*, *34*, *40*, *53*, *58*). One of the most widely accepted explanation is that the interfacial water, representing an ordered layer of water molecules on the surface, exhibits very low refractive index due to suppressed rotation at the solid-liquid interface. To incorporate the above model, we first attempt to determine thickness and refractive index of the interfacial water on the sidewall of our metal nanogap. From a hybrid-type approach with molecular dynamics and density functional theory calculations (see the Supplementary Materials, fig. S8), we estimate 0.75 nm as the thickness of the interfacial water layer. Here, we assumed that the gold surface is hydrophilic judging from the contact angle measurement; however, hydrophilicity of the surface minimally affects the calculated thickness of the interfacial water layer (see the Supplementary Materials, fig. S7). Therefore, the spectral response of a 2-nm gap will be

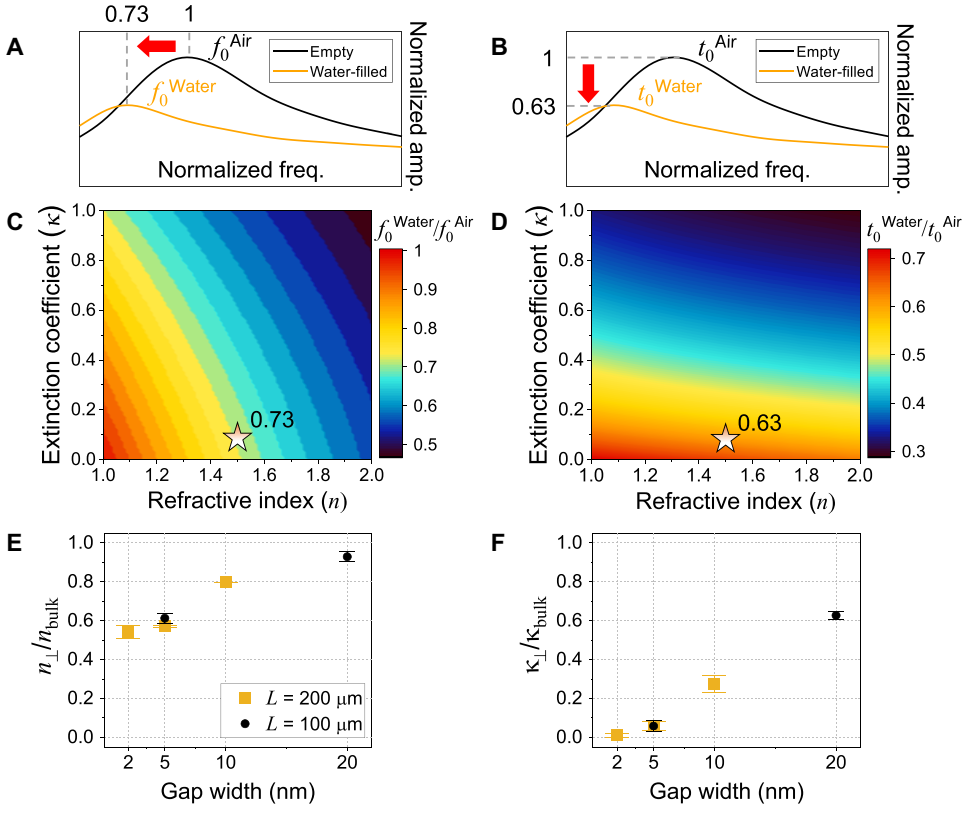

Fig. 4. Quantitative estimation of the complex refractive index, $\tilde{n} = n + i\kappa$, of gap-filling water within a gap width range of 2 to 20 nm. (**A** and **B**) The measured relative resonance frequency [$f_0^{Water} / f_0^{Air} = 0.73$; (A)] and measured relative peak amplitude [$t_0^{Water} / t_0^{Air} = 0.63$; (B)] for the water-filled nanogap loop with respect to those of an empty gap (i. e., $n = 1$, $\kappa = 0$). (**C** and **D**) The 2D maps of the relative resonance peak amplitude [in (C)] and the relative resonance frequency [in (D)] with respect to those of an empty gap. The gap width (w) is 5 nm, and the loop length [$L = 2(L_x + L_y)$] is 200 μm. The star symbols in (C) and (D) indicate the estimated refractive index of gap-filling water, satisfying both the experimentally obtained relative resonance frequency and relative peak amplitude simultaneously. (**E** and **F**) Estimated relative refractive indices [$n_\perp/n_{bulk}$; (E)] and relative extinction coefficients [$\kappa_\perp / \kappa_{bulk}$; (F)] of the nanoconfined water at each resonance ($f_{L=200\ \mu m}^{w=2\ nm} = 0.24$ THz, $f_{L=200\ \mu m}^{w=5\ nm} = 0.23$ THz, $f_{L=200\ \mu m}^{w=10\ nm} = 0.32$ THz, $f_{L=100\ \mu m}^{w=5\ nm} = 0.46$ THz, $f_{L=100\ \mu m}^{w=20\ nm} = 0.7$ THz) as a function of the gap width. Both $n_\perp$ and $\kappa_\perp$ are x-direction refractive indices, being perpendicular to the metal surface, namely, the sidewall of the first metal pattern shown in Fig. 2A.

dominated by the refractive indices of the interfacial water whose thickness is 0.75 nm by 2 = 1.5 nm; $\tilde{n}_{\perp}$ estimated from the 2-nm gap sample sets an upper limit for the refractive index of the interfacial water, i.e., $n_{\text{upper}} = 1.41 + i0$. If we follow the convention to use refractive index of water at visible frequencies (*52*) as the lower bound $n_{\text{lower}} \simeq \sqrt{\varepsilon_{\infty}} = 1.33$, we continue our discussion assuming $n_i = 1.37 + i0$ as a representative value for the refractive index of interfacial water.

Next, we incorporate an effective medium theory combined with a three-layer capacitor model with two interfacial layers and one residual layer, and assumed that the decrease in dielectric permittivity is primarily attributed to the interfacial layer (*59*). However, we find that this three-layer model, which is widely accepted at the static regime, is inadequate to explain the observed decrease in dielectric permittivity in THz frequencies due to the intricate collective phenomena involved (*58*) (see fig. S9 and Supplementary Text in the Supplementary Materials). This implies that the residual layer, generally recognized as a quasi-bulk water, also undergoes a substantial reduction in THz refractive indices at gap widths as large as 10 nm, in sharp contrast to the static regime. As shown in fig. S9 (C and F), the complex refractive indices of the residual water decrease gradually with smaller gap widths, with the 2-nm gap reducing to 60 and 0% of its bulk counterpart's real and imaginary parts, respectively.

To understand the underlying physics behind this phenomenon, we refer to recent studies which predict that confinement may lead to suppression of VDOS at low-energy limit, thereby leading to a low dielectric permittivity (*22*–*24*, *60*). As the frequency range of our interest (0.1 to 1.5 THz) may be considered sufficiently low in terms of equivalent energy (0.4 to 6 meV), we used this theory (*60*) to formulate a model to qualitatively explain the reduced dielectric permittivity of nanoconfined water. First, we have assumed that (i) permittivity of water may be expressed as a sum of multiple Lorentzian oscillators which account for vibrational modes of water and that (ii) the number of oscillators decrease at narrower gaps because of the suppression of the vibrational modes (*60*). Because of the relatively small dispersion of water and for the sake of simplicity, we further assumed that the VDOS would be uniform over the entire spectrum of interest, allowing the permittivity to be expressed as a sum of identical Lorentzian oscillators equally spaced in the spectrum. By denoting the number of oscillators as *P*, suppression of vibrational modes may directly be converted into a decrease in *P*, which will determine the permittivity spectrum of the nanoconfined water accordingly. Our first step was to obtain relevant parameters for the Lorentzian oscillators by fitting the experimentally obtained permittivity spectra of bulk water with our model, which will be called the VDOS model. The number of vibrational modes for bulk water is denoted as P_0 and will be used as a reference when analyzing the data from nanoconfined water. Figure 5 (A to D) shows the experimentally measured transmission spectra for water-filled nanogaps with different gap widths, as well as fitted curves obtained from the VDOS model with *P* as one of the fitting parameters. On the basis of the fitted data, we find that the number of vibrational modes of nanoconfined water reduces to 85, 34, 11, and 5% of those of bulk water, respectively, at the gap widths of 20, 10, 5, and 2 nm. The decreased permittivity of nanoconfined water may therefore be explained by suppressed vibrational modes at narrower gaps, as reported by the earlier works (*22*, *24*). Figure S10 in the Supplementary Materials shows the resulting frequency-dependent dielectric permittivity spectra of nanoconfined water obtained from the VDOS model. It is noteworthy that, at a higher degree of confinement, the dispersion is substantially reduced, which is due to a smaller number of Lorentzian oscillators contributing to the total permittivity. The number of vibrational modes *P* as a function of the gap width (*w*) is plotted in Fig. 5E. It is clear from the analysis that the trend is linear, which implies that the confinement effect may be volumetric, i.e. $P \sim w \sim V$, where *V* is the confinement volume. This is qualitatively consistent with a previous study (*24*) where the authors express the number of vibrational states at a specific wave number *k* as $\mathrm{d}n = V_k^{-1} 4\pi k^2 \mathrm{d}k$, where $V_k = (2\pi)^3 / V$ is the *k*-space volume occupied by a single wave vector. While more rigorous and quantitative studies are required to understand the nanoconfinement effect, we were able to demonstrate that the decreased permittivity of nanoconfined water can be explained in the context of a reduced number of vibrational modes.

Ice-to-water phase transition under nanoconfinement

We can draw a parallel between the lowering refractive index observed in nanoconfined water and the changing refractive index during the phase transition from liquid water to solid ice. In the solid state of ice, the spacing between hydrogen bonds becomes fixed, causing water molecules to align in a structured manner. This arrangement results in lower refractive indices compared to liquid water. Therefore, temperature-dependent THz transmission measurements on water-filled nanogaps can provide additional insight on the gap width–dependent collective dynamics of water molecules.

Figure 6A shows the measured THz time traces of water-filled nanogaps with the gap widths of 1.5, 5, and 20 nm when the temperatures are 250 and 290 K, and Fig. 6 (B to D) shows the corresponding THz spectra. The spectra exhibit a decrease in amplitude and a spectral red shift as the temperature rises from 250 K, surpassing 273 K, to 290 K (fig. S11 in the Supplementary Materials). This is an expected trend as refractive index of bulk water is larger than that of the bulk ice (~1.77). What should be noted, however, is that the spectral shift is smaller in narrower gaps, which is counterintuitive because narrower gaps are much more sensitive to changes in dielectric environment within the gap. This implies that dielectric properties of nanoconfined water and ice are similar. The series of transmitted amplitude changes for each sample is compared in Fig. 6E as a function of temperature. For 1.5-nm gap, the amplitude change during the phase transition was almost negligible, which is because 1.5-nm-thick nanoconfined water consists exclusively of the immobile interfacial layers. For 5- and 20-nm gaps, we find that the amplitude change for 5-nm gap is only half as large as observed in the 20-nm gap, which implies that the nanoconfined water is more "ice-like" in a 5-nm gap. The ice-like nature of the nanoconfined water may be better visualized by comparing the results with simulations assuming bulk water and ice filling the gap, as shown in Fig. 6F. While the observed amplitude changes in the 20-nm gap are relatively consistent with the calculations, the changes in the 5- and 1.5-nm gaps deviate by approximately 3 and 15 times from the predicted value with the bulk values. Accordingly, at THz frequencies, the optical properties of nanoconfined water deviate substantially from those of bulk counterpart, suggesting that suppressed collective dynamics of water molecules are observed over longer distances than we expected.

We may also determine THz refractive indices of the "nanoconfined ice" and compare them with the bulk counterpart, as we did with liquid water. For gap widths of 5 and 20 nm, we estimate indices

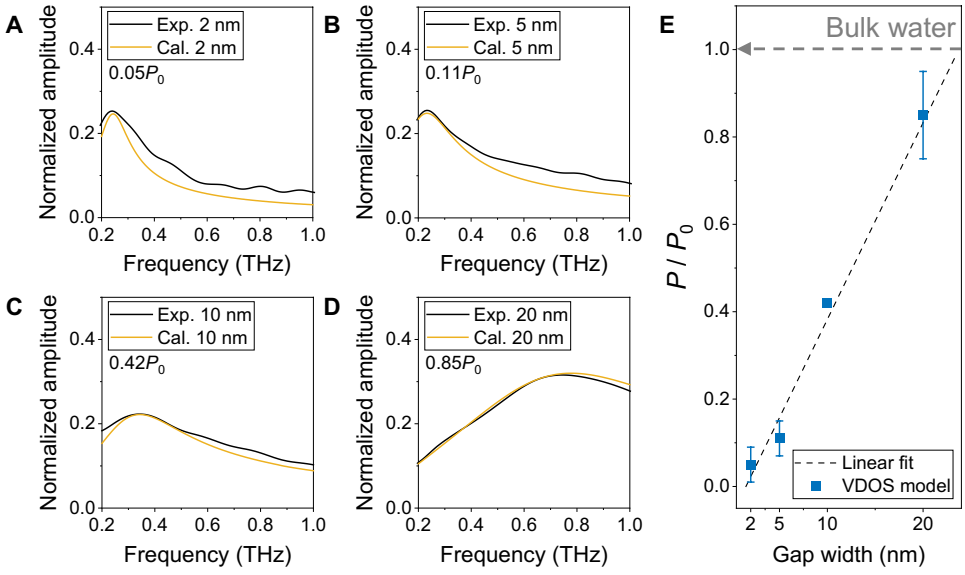

Fig. 5. Suppressed vibrational modes of water confined in nanometer gaps. (**A** to **D**) The measured THz transmission spectra of water-filled nanogaps with gap widths of 2, 5, 10, and 20 nm (black line), along with the calculated THz transmission spectra obtained by inserting the dielectric constant spectra derived from theory into the coupled-mode method (orange line). P_0 represents the number of vibrational modes of bulk water, and the number of vibrational modes, P, that best matches each spectrum, are indicated in the plot. (**E**) The relationship between the gap width and number of vibrational modes P. The error bars represent the range of P values that can vary because of experimental error.

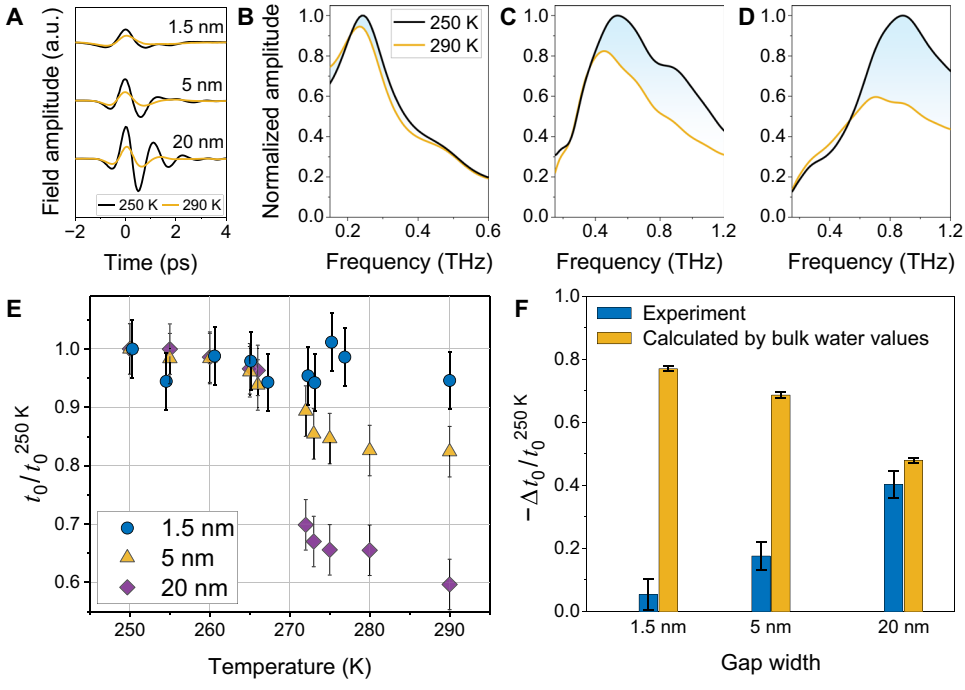

Fig. 6. Temperature-dependent THz-TDS with water confined in metal nanogaps. (**A**) Time traces of the nanoconfined water from ice to liquid water phase for the gap widths of 1.5, 5, and 20 nm, respectively. The time traces are vertically offset for clarity. (**B** to **D**) Fourier-transformed transmitted amplitude spectra in frequency domain from ice to water for (B) 1.5-, (C) 5-, and (D) 20-nm gaps. (**E**) Relative resonance peak amplitudes depending on the temperature for 1.5-nm (circle dot), 5-nm (triangle dot), and 20-nm (diamond dot) gaps. All the data have been normalized by the peak amplitude at 250 K. (**F**) Comparison of the relative peak amplitude changes between the two phases of liquid water and ice for gap widths of 1.5, 5, and 20 nm. Blue bars, experimental results by temperature-dependent THz-TDS. Orange bars, calculation results with the bulk water using the coupled-mode method.

of the nanoconfined ice as 1.2 ($w = 5$ nm) and 1.7 ($w = 20$ nm) with a nearly zero imaginary part. Compared to the THz refractive index of bulk ice of $\tilde{n} = 1.77 + i0$, we can conclude that the 20-nm-thick ice is almost close to bulk ice, while the index of 5-nm-thick ice is strongly suppressed by the nanoconfinement effect. This finding is in line with a recent report in which the VDOS of nanoconfined solids is found to follow $\sim\omega^3$ in the low-frequency limit, while the dependence is $\sim\omega^2$ for normal solids (*24*). As a result, nanoconfinement suppresses vibrational modes and reduces the dielectric permittivity of ice in a similar manner to nanoconfined water.

DISCUSSION

In this study, we performed gap width–dependent THz transmission measurements on water-filled metal nanogap to determine refractive indices of the nanoconfined water at THz frequencies. We observed a considerable decrease in both real and imaginary refractive indices of the nanoconfined water compared to those of bulk water, but with a trend that could not be explained sufficiently with the three-layer capacitor model proposed in the static regime. Using the VDOS model, we attribute this deviation to the suppressed dynamics of the long-range correlation of hydrogen bond networks corresponding to the THz frequency regime under extremely confined volume. This constraint leads to a reduction in the THz permittivity of the "non-interfacial" water, as demonstrated through temperature-dependent measurements. Even though this study focuses on THz frequencies, the scope of the study can be expanded to visible, infrared, and even microwave frequencies simply by altering the dimensions of the metal nanogaps. It is also possible to study interfacial dynamics of water molecules on different metals or even on dielectrics or self-assembled molecules by coating the layers after fully etching the gap. Furthermore, if the water-filled gap can be realized at subnanometer gap widths (*51*), then our understanding of nanoconfined water may be extended to much more exotic phenomena, such as various phases of monolayer (*16*, *61*) and an anomalous shift of phase transition temperatures (*20*). Therefore, our scheme provides a previously unknown method to study and use water-mediated processes such as protein folding, lipid rafts, and molecular recognition.

MATERIALS AND METHODS

Fabrication of water-filled nanogap loops

First, we cleaned a 500-μm-thick silicon substrate using acetone and isopropyl alcohol in an ultrasonic environment to remove any particles. We then applied image reversal photoresist (AZ 5214E) onto the silicon wafer at 4000 rpm for 30 s, followed by a soft bake at 105°C for 90 s to eliminate residual solvent. The coated sample was exposed to ultraviolet light with an intensity of 10 mW/cm^2 and a wavelength of 365 nm (i-line) for 5 s using a MIDAS MA-6 mask aligner. After the reversal bake and flood exposure, we developed the sample with MIF 300 developer for 120 s and rinsed it with DI water for an additional 120 s. Subsequently, we deposited a 200-nm-thick layer of gold and a 2-nm-thick layer of chromium (Cr) using an electron beam evaporator and then removed any remaining photoresist with acetone. Using an ALD system (Lucida 100), we then deposited a conformal layer of Al_2O_3, varying from 2 to 20 nm, using trimethylaluminum as the precursor and DI water as the reactor, controlling the thickness by adjusting the number of cycles, all at a temperature of 200°C. The deposition rate of Al_2O_3 was 1.1 Å per cycle, with the thickness confirmed using ellipsometry. Afterwards, a 200-nm-thick layer of gold was deposited on top of the sample, which filled the empty region and defined the metal-insulator-metal gap. Excess gold that was deposited on top of the first gold layer was subsequently removed using adhesive tape. To achieve a smoother surface, we polished the nanogap loops' exteriors using an Ar-ion miller at an oblique angle of 85° for 5 min. Following this, we etched the Al_2O_3 inside the nanogaps using a 1 M KOH solution, varying the etching time from 1 min for the 2-nm gap to 10 min for the 20-nm gap, depending on the gap width. Following the etching process, we immediately transferred the KOH bath to a DI water (resistance = 18.2 megohm·cm) reservoir, allowing DI water to dilute the KOH solution and simultaneously fill the gap. Last, we sealed the water-filled nanogap loops using a sapphire cover (650 μm) with double-sided Kapton tapes (100 μm) as a spacer within a DI water bath. For low-temperature measurements, we additionally sealed sidewalls of the sample using GE varnish, preventing the vaporization of water molecules under ultrahigh-vacuum conditions.

THz time-domain spectroscopy

To investigate the dynamics of water molecules within nanogaps, we used transmission-type THz-TDS. We used a commercial Ti:sapphire oscillator system (Synergy BB, Spectra-Physics) operating at a central wavelength of 780 nm, producing sub–10-fs pulse widths with a repetition rate of 75.1 MHz. For THz generation, we used a commercial GaAs photoconductive antenna (Tera-SED3, Laser Quantum) with a field amplitude of 300 V/cm. The resulting THz pulse spanned a spectral range from 0.1 to 3 THz and was guided using a series of off-axis parabolic mirrors. The focused THz pulse, with a beam size of 2 mm, was directed onto the water-filled nanogap loops. Detection of the transmitted THz pulse was accomplished through an electro-optic sampling method using a 1-mm-thick (110) ZnTe crystal. To mitigate water vapor absorption effects at THz frequencies, we maintained a dry air purging system throughout the experiment.

Temperature-dependent measurement

We used a liquid helium (He) flowed cryostat (MicrostatHe2, Oxford Instruments) to confirm the phase transition of water within the nanogap. To avoid multiple reflections of THz waves, we used a transparent 3-mm-thick Polymethylpentene window optimized for THz frequencies. Furthermore, we designed a customized holder from oxygen-free copper, renowned for its superior thermal conductivity. This holder incorporated a temperature sensor (DT-670, Lakeshore) to ensure precise temperature measurement of the sample. Heat transfer was facilitated through a wire, with a cryogenic manganin wire of exceptionally low thermal conductivity used to impede heat flow. A segment of this wire was attached to a cold finger for effective heat anchoring. This meticulous arrangement yielded a temperature difference between the cold finger and the sample part within a remarkably tight ±0.1-K range in the low-temperature domain. For affixing the sample to the specific holder, we used GE varnish, allowing ample drying time of 24 hours before loading it into the cryostat. All low-temperature measurements were carried out under high-vacuum conditions ($<8.5 \times 10^{-7}$ mbar) to prevent the freezing of water vapor.

Supplementary Materials

This PDF file includes:

Supplementary Text
Figs. S1 to S11
Tables S1 and S2
References

REFERENCES AND NOTES

1. M. C. Bellissent-Funel, A. Hassanali, M. Havenith, R. Henchman, P. Pohl, F. Sterpone, D. van der Spoel, Y. Xu, A. E. Garcia, Water Determines the Structure and Dynamics of Proteins. *Chem. Rev.* **116**, 7673–7697 (2016).
2. M. Santra, A. Seal, K. Bhattacharjee, S. Chakrabarty, Structural and dynamical heterogeneity of water trapped inside Na^+ –pumping KR2 rhodopsin in the dark state. *J. Chem. Phys.* **154**, 215101 (2021).
3. Y. Nakajima, A. Momotake, A. Suzuki, S. Neya, Y. Yamamoto, Nature of a H_2O Molecule Confined in the Hydrophobic Interface between the Heme and G-Quartet Planes in a Heme-DNA Complex. *Biochemistry* **61**, 523–534 (2022).
4. D. Hegemann, N. Hocquard, M. Heuberger, Nanoconfined water can orient and cause long-range dipolar interactions with biomolecules. *Sci. Rep.* **7**, 17852 (2017).
5. O. Bunjes, D. Hedman, A. Rittmeier, L. A. Paul, I. Siewert, F. Ding, M. Wenderoth, Making and breaking of chemical bonds in single nanoconfined molecules. *Sci. Adv.* **8**, eabq7776 (2022).
6. W. J. Mu, Z. Ji, M. Zhou, J. Wu, Y. Lin, Y. Qiao, Membrane-confined liquid-liquid phase separation toward artificial organelles. *Sci. Adv.* **7**, eabf9000 (2021).
7. P. F. Zhan, A. Peil, Q. Jiang, D. Wang, S. Mousavi, Q. Xiong, Q. Shen, Y. Shang, B. Ding, C. Lin, Y. Ke, N. Liu, Recent Advances in DNA Origami-Engineered Nanomaterials and Applications. *Chem. Rev.* **123**, 3976–4050 (2023).
8. P. Biswas, D. Sen, M. Prasher, S. K. Sarkar, K. Dasgupta, Confinement driven anomalous freezing in nano porous spray dried microspheres. *Nanotechnology* **32**, 385707 (2021).
9. E. Chiavazzo, M. Fasano, P. Asinari, P. Decuzzi, Scaling behaviour for the water transport in nanoconfined geometries. *Nat. Commun.* **5**, 3565 (2014).
10. D. J. Bonthuis, S. Gekle, R. R. Netz, Dielectric Profile of Interfacial Water and its Effect on Double-Layer Capacitance. *Phys. Rev. Lett.* **107**, 166102 (2011).
11. B. Moeremans, H. W. Cheng, Q. Hu, H. F. Garces, N. P. Padture, F. U. Renner, M. Valtiner, Lithium-ion battery electrolyte mobility at nano-confined graphene interfaces. *Nat. Commun.* **7**, 12693 (2016).
12. M. Kasuya, D. Kubota, S. Fujii, K. Kurihara, Nano-confined electrochemical reaction studied by electrochemical surface forces apparatus. *Faraday Discuss.* **233**, 206–221 (2022).
13. M. Beaumont, P. Jusner, N. Gierlinger, A. W. T. King, A. Potthast, O. J. Rojas, T. Rosenau, Unique reactivity of nanoporous cellulosic materials mediated by surface-confined water. *Nat. Commun.* **12**, 2513 (2021).
14. H. Zhu, A. Ghoufi, A. Szymczyk, B. Balannec, D. Morineau, Anomalous Dielectric Behavior of Nanoconfined Electrolytic Solutions. *Phys. Rev. Lett.* **109**, 107801 (2012).
15. R. Esquivel-Sirvent, Anomaly of the dielectric function of water under confinement and its role in van der Waals interactions. *Phys. Rev. E* **102**, 042609 (2020).
16. V. Kapil, C. Schran, A. Zen, J. Chen, C. J. Pickard, A. Michaelides, The first-principles phase diagram of monolayer nanoconfined water. *Nature* **609**, 512–516 (2022).
17. J. J. Gilijamse, A. J. Lock, H. J. Bakker, Dynamics of confined water molecules. *Proc. Natl. Acad. Sci. U.S.A.* **102**, 3202–3207 (2005).
18. T. D. Li, J. P. Gao, R. Szoszkiewicz, U. Landman, E. Riedo, Structured and viscous water in subnanometer gaps. *Phys. Rev. B* **75**, 115415 (2007).
19. P. Boynton, M. Di Ventra, Probing Water Structures in Nanopores Using Tunneling Currents. *Phys. Rev. Lett.* **111**, 216804 (2013).
20. K. V. Agrawal, S. Shimizu, L. W. Drahushuk, D. Kilcoyne, M. S. Strano, Observation of extreme phase transition temperatures of water confined inside isolated carbon nanotubes. *Nat. Nanotechnol.* **12**, 267–273 (2017).
21. Y. Ishii, N. Matubayasi, G. Watanabe, T. Kato, H. Washizu, Molecular insights on confined water in the nanochannels of self-assembled ionic liquid crystal. *Sci. Adv.* **7**, eabf0669 (2021).
22. A. E. Phillips, M. Baggioli, T. W. Sirk, K. Trachenko, A. Zaccone, Universal L^{-3} finite-size effects in the viscoelasticity of amorphous systems. *Phys. Rev. Mater.* **5**, 035602 (2021).
23. A. Zaccone, L. Noirez, Universal $G' \sim L^{-3}$ Law for the Low-Frequency Shear Modulus of Confined Liquids. *J. Phys. Chem. Lett.* **12**, 650–657 (2021).
24. Y. X. Yu, C. Yang, M. Baggioli, A. E. Phillips, A. Zaccone, L. Zhang, R. Kajimoto, M. Nakamura, D. Yu, The ω^3 scaling of the vibrational density of states in quasi-2D nanoconfined solids. *Nat. Commun.* **13**, 3649 (2022).
25. D. Ortiz-Young, H. C. Chiu, S. Kim, K. Voïtchovsky, E. Riedo, The interplay between apparent viscosity and wettability in nanoconfined water. *Nat. Commun.* **4**, 2482 (2013).
26. A. Zaccone, K. Trachenko, Explaining the low-frequency shear elasticity of confined liquids. *Proc. Natl. Acad. Sci. U.S.A.* **117**, 19653–19655 (2020).
27. D. Shin, J. Hwang, W. Jhe, Ice-VII-like molecular structure of ambient water nanomeniscus. *Nat. Commun.* **10**, 286 (2019).
28. A. Zaccone, M. Baggioli, Universal law for the vibrational density of states of liquids. *Proc. Natl. Acad. Sci. U.S.A.* **118**, e2022303118 (2021).
29. S. Toda, S. Shigeto, Hydrogen Bonded Structures of Confined Water Molecules and Electric Field Induced Shift of Their Equilibrium Revealed by IR Electroabsorption Spectroscopy. *J. Phys. Chem. B* **121**, 5573–5581 (2017).
30. S. Varghese, S. K. Kannam, J. S. Hansen, S. P. Sathian, Effect of Hydrogen Bonds on the Dielectric Properties of Interfacial Water. *Langmuir* **35**, 8159–8166 (2019).
31. H. Jalali, H. Ghorbanfekr, I. Hamid, M. Neek-Amal, R. Rashidi, F. M. Peeters, Out-of-plane permittivity of confined water. *Phys. Rev. E* **102**, 022803 (2020).
32. D. Vanzo, D. Bratko, A. Luzar, Nanoconfined water under electric field at constant chemical potential undergoes electrostriction. *J. Chem. Phys.* **140**, 074710 (2014).
33. F. Foglia, A. J. Clancy, J. Berry-Gair, K. Lisowska, M. C. Wilding, T. M. Suter, T. S. Miller, K. Smith, F. Demmel, M. Appel, V. G. Sakai, A. Sella, C. A. Howard, M. Tyagi, F. Corà, P. F. McMillan, Aquaporin-like water transport in nanoporous crystalline layered carbon nitride. *Sci. Adv.* **6**, eabb6011 (2020).
34. L. Fumagalli, A. Esfandiar, R. Fabregas, S. Hu, P. Ares, A. Janardanan, Q. Yang, B. Radha, T. Taniguchi, K. Watanabe, G. Gomila, K. S. Novoselov, A. K. Geim, Anomalously low dielectric constant of confined water. *Science* **360**, 1339–1342 (2018).
35. M. A. Belyanchikov, E. S. Zhukova, S. Tretiak, A. Zhugayevych, M. Dressel, F. Uhlig, J. Smiatek, M. Fyta, V. G. Thomas, B. P. Gorshunov, Vibrational states of nano-confined water molecules in beryl investigated by first-principles calculations and optical experiments. *Phys. Chem. Chem. Phys.* **19**, 30740–30748 (2017).
36. P. Gorshunov, V. I. Torgashev, E. S. Zhukova, V. G. Thomas, M. A. Belyanchikov, C. Kadlec, F. Kadlec, M. Savinov, T. Ostapchuk, J. Petzelt, J. Prokleška, P. V. Tomas, E. V. Pestrjakov, D. A. Fursenko, G. S. Shakurov, A. S. Prokhorov, V. S. Gorelik, L. S. Kadyrov, V. V. Uskov, R. K. Kremer, M. Dressel, Incipient ferroelectricity of water molecules confined to nano-channels of beryl. *Nat. Commun.* **7**, 12842 (2016).
37. J. Q. Zhang, D. Grischkowsky, Terahertz time-domain spectroscopy of submonolayer water adsorption in hydrophilic silica aerogel. *Opt. Lett.* **29**, 1031–1033 (2004).
38. J. Q. Zhang, D. Grischkowsky, Waveguide terahertz time-domain spectroscopy of nanometer water layers. *Opt. Lett.* **29**, 1617–1619 (2004).
39. J. Jeong, H. S. Yun, D. Kim, K. S. Lee, H. K. Choi, Z. H. Kim, S. W. Lee, D. S. Kim, High Contrast Detection of Water-Filled Terahertz Nanotrenches. *Adv. Opt. Mater.* **6**, 1800582 (2018).
40. T. H. H. Le, A. Morita, T. Tanaka, Refractive index of nanoconfined water reveals its anomalous physical properties. *Nanoscale Horiz.* **5**, 1016–1024 (2020).
41. J. Jeong, D. S. Kim, H. R. Park, Beyond-hot-spot absorption enhancement on top of terahertz nanotrenches. *Nanophotonics* **11**, 3159–3167 (2022).
42. J. Balajka, J. Pavelec, M. Komora, M. Schmid, U. Diebold, Apparatus for dosing liquid water in ultrahigh vacuum. *Rev. Sci. Instrum.* **89**, 083906 (2018).
43. B. Slater, A. Michaelides, Surface premelting of water ice. *Nat. Rev. Chem.* **3**, 172–188 (2019).
44. X. S. Chen, H.-R. Park, M. Pelton, X. Piao, N. C. Lindquist, H. Im, Y. J. Kim, J. S. Ahn, K. J. Ahn, N. Park, D.-S. Kim, S.-H. Oh, Atomic layer lithography of wafer-scale nanogap arrays for extreme confinement of electromagnetic waves. *Nat. Commun.* **4**, 2361 (2013).
45. J. Jeong, D. Kim, M. Seo, D. S. Kim, Strongly Localized ohmic Absorption of Terahertz Radiation in Nanoslot Antennas. *Nano Lett.* **19**, 9062–9068 (2019).
46. D. Kim, J. Jeong, G. Choi, Y. M. Bahk, T. Kang, D. Lee, B. Thusa, D. S. Kim, Giant Field Enhancements in Ultrathin Nanoslots above 1 Terahertz. *ACS Photonics* **5**, 1885–1890 (2018).
47. G. Ji, H. S. Kim, S. H. Cha, H.-T. Lee, H. J. Kim, S. W. Lee, K. J Ahn, K.-H. Kim, Y. H. Ahn, H.-R. Park, Terahertz virus-sized gold nanogap sensor. *Nanophotonics* **12**, 147–154 (2023).
48. S. Baek, S. H. Park, D. Oh, K. Lee, S. Lee, H. Lim, T. Ha, H. S. Park, S. Zhang, L. Yang, B. Min, T. T. Kim, Non-Hermitian chiral degeneracy of gated graphene metasurfaces. *Light Sci. Appl.* **12**, 87 (2023).
49. L. Q. Cong, Y. K. Srivastava, H. Zhang, X. Zhang, J. Han, R. Singh, All-optical active THz metasurfaces for ultrafast polarization switching and dynamic beam splitting. *Light Sci. Appl.* **7**, 28 (2018).
50. J. Qin, S. Jiang, Z. Wang, X. Cheng, B. Li, Y. Shi, D. P. Tsai, A. Q. Liu, W. Huang, W. Zhu, Metasurface Micro/Nano-Optical Sensors: Principles and Applications. *ACS Nano* **16**, 11598–11618 (2022).
51. Y. M. Bahk, B. J. Kang, Y. S. Kim, J. Y. Kim, W. T. Kim, T. Y. Kim, T. Kang, J. Rhie, S. Han, C. H. Park, F. Rotermund, D. S. Kim, Electromagnetic Saturation of Angstrom-Sized Quantum Barriers at Terahertz Frequencies. *Phys. Rev. Lett.* **115**, 125501 (2015).
52. T. Fukasawa, T. Sato, J. Watanabe, Y. Hama, W. Kunz, R. Buchner, Relation between dielectric and low-frequency Raman spectra of hydrogen-bond liquids. *Phys. Rev. Lett.* **95**, 197802 (2005).
53. W. P. Qi, J. Chen, J. Yang, X. Lei, B. Song, H. Fang, Anisotropic Dielectric Relaxation of the Water Confined in Nanotubes for Terahertz Spectroscopy Studied by Molecular Dynamics Simulations. *J. Phys. Chem. B* **117**, 7967–7971 (2013).
54. I. Popov, P. Ben Ishai, A. Khamzin, Y. Feldman, The mechanism of the dielectric relaxation in water. *Phys. Chem. Chem. Phys.* **18**, 13941–13953 (2016).
55. D. C. Elton, The origin of the Debye relaxation in liquid water and fitting the high frequency excess response. *Phys. Chem. Chem. Phys.* **19**, 18739–18749 (2017).
56. H. Zhao, Y. Tan, L. Zhang, R. Zhang, M. Shalaby, C. Zhang, Y. Zhao, X. C. Zhang, Ultrafast hydrogen bond dynamics of liquid water revealed by terahertz-induced transient birefringence. *Light Sci. Appl.* **9**, 136 (2020).
57. J. Jeong, H. Yang, S. Park, Y. D. Park, D. S. Kim, Ultra-Narrow Metallic Nano-Trenches Realized by Wet Etching and Critical Point Drying. *Nanomaterials* **11**, 783 (2021).

58. J. F. Olivieri, J. T. Hynes, D. Laage, Confined Water's Dielectric Constant Reduction Is Due to the Surrounding Low Dielectric Media and Not to Interfacial Molecular Ordering. *J. Phys. Chem. Lett.* **12**, 4319–4326 (2021).
59. S. Giordano, Dielectric and Elastic Characterization of Nonlinear Heterogeneous Materials. *Materials* **2**, 1417–1479 (2009).
60. B. Y. Cui, R. Milkus, A. Zaccone, Direct link between boson-peak modes and dielectric α-relaxation in glasses. *Phys. Rev. E* **95**, 022603 (2017).
61. B. Lin, J. Jiang, X. C. Zeng, L. Li, Temperature-pressure phase diagram of confined monolayer water/ice at first-principles accuracy with a machine-learning force field. *Nat. Commun.* **14**, 4110 (2023).
62. M. A. Seo, H. R. Park, S. M. Koo, D. J. Park, J. H. Kang, O. K. Suwal, S. S. Choi, P. C. M. Planken, G. S. Park, N. K. Park, Q. H. Park, D. S. Kim, Terahertz field enhancement by a metallic nano slit operating beyond the skin-depth limit. *Nat. Photonics* **3**, 152–156 (2009).
63. A. N. Tcypkin, M. V. Melnik, M. O. Zhukova, I. O. Vorontsova, S. E. Putilin, S. A. Kozlov, X. C. Zhang, High Kerr nonlinearity of water in THz spectral range. *Opt. Express* **27**, 10419–10425 (2019).
64. F. J. Garcia-Vidal, E. Moreno, J. A. Porto, L. Martin-Moreno, Transmission of light through a single rectangular hole. *Phys. Rev. Lett.* **95**, 103901 (2005).
65. F. J. Garcia-Vidal, L. Martin-Moreno, E. Moreno, L. K. S. Kumar, R. Gordon, Transmission of light through a single rectangular hole in a real metal. *Phys. Rev. B* **74**, 153411 (2006).
66. J. Jeong, D. Kim, H. R. Park, T. Kang, D. Lee, S. Kim, Y. M. Bahk, D. S. Kim, Anomalous extinction in index-matched terahertz nanogaps. *Nanophotonics* **7**, 347–354 (2018).
67. H. T. Lee, G. S. Ji, J. Y. Oh, C. W. Seo, B. W. Kang, K. W. Kim, H. R. Park, Measuring Complex Refractive Indices of a Nanometer-Thick Superconducting Film Using Terahertz Time-Domain Spectroscopy with a 10 Femtoseconds Pulse Laser. *Crystals* **11**, 651 (2021).
68. C. A. Ward, M. R. Sasges, Effect of gravity on contact angle: A theoretical investigation. *J. Chem. Phys.* **109**, 3651–3660 (1998).
69. M. R. Sasges, C. A. Ward, Effect of gravity on contact angle: An experimental investigation. *J. Chem. Phys.* **109**, 3661–3670 (1998).
70. R. N. Wenzel, Resistance of solid surfaces to wetting by water. *Ind. Eng. Chem. Res.* **28**, 988–994 (1936).
71. C. Sendner, D. Horinek, L. Bocquet, R. R. Netz, Interfacial Water at Hydrophobic and Hydrophilic Surfaces: Slip, Viscosity, and Diffusion. *Langmuir* **25**, 10768–10781 (2009).
72. T. Laino, F. Mohamed, A. Laio, M. Parrinello, An efficient real space multigrid QM/MM electrostatic coupling. *J. Chem. Theory Comput.* **1**, 1176–1184 (2005).
73. S. Pronk, S. Páll, R. Schulz, P. Larsson, P. Bjelkmar, R. Apostolov, M. R. Shirts, J. C. Smith, P. M. Kasson, D. van der Spoel, B. Hess, E. Lindahl, GROMACS 4.5: a high-throughput and highly parallel open source molecular simulation toolkit. *Bioinformatics* **29**, 845–854 (2013).
74. T. D. Kuhne, M. Iannuzzi, M. Del Ben, V. V. Rybkin, P. Seewald, F. Stein, T. Laino, R. Z. Khaliullin, O. Schütt, F. Schiffmann, D. Golze, J. Wilhelm, S. Chulkov, M. H. Bani-Hashemian, V. Weber, U. Borštnik, M. Taillefumier, A. S. Jakobovits, A. Lazzaro, H. Pabst, T. Müller, R. Schade, M. Guidon, S. Andermatt, N. Holmberg, G. K. Schenter, A. Hehn, A. Bussy, F. Belleflamme, G. Tabacchi, A. Glöß, M. Lass, I. Bethune, C. J. Mundy, C. Plessl, M. Watkins, J. V. Vondele, M. Krack, J. Hutter, CP2K: An electronic structure and molecular dynamics software package - Quickstep: Efficient and accurate electronic structure calculations. *J. Chem. Phys.* **152**, 194103 (2020).
75. J. P. Perdew, K. Burke, M. Ernzerhof, Generalized gradient approximation made simple. *Phys. Rev. Lett.* **77**, 3865–3868 (1996).
76. W. L. Jorgensen, J. Chandrasekhar, J. D. Madura, R. W. Impey, M. L. Klein, Comparison of Simple Potential Functions for Simulating Liquid Water. *J. Chem. Phys.* **79**, 926–935 (1983).
77. V. Hornak, R. Abel, A. Okur, B. Strockbine, A. Roitberg, C. Simmerling, Comparison of multiple amber force fields and development of improved protein backbone parameters. *Proteins* **65**, 712–725 (2006).
78. A. Jain, S. P. Ong, G. Hautier, W. Chen, W. D. Richards, S. Dacek, S. Cholia, D. Gunter, D. Skinner, G. Ceder, K. A. Persson, Commentary: The Materials Project: A materials genome approach to accelerating materials innovation. *APL Mater.* **1**, 011002 (2013).
79. P. Giannozzi, S. Baroni, N. Bonini, M. Calandra, R. Car, C. Cavazzoni, D. Ceresoli, G. L. Chiarotti, M. Cococcioni, I. Dabo, A. Dal Corso, S. de Gironcoli, S. Fabris, G. Fratesi, R. Gebauer, U. Gerstmann, C. Gougoussis, A. Kokalj, M. Lazzeri, L. Martin-Samos, N. Marzari, F. Mauri, R. Mazzarello, S. Paolini, A. Pasquarello, L. Paulatto, C. Sbraccia, S. Scandolo, G. Sclauzero, A. P. Seitsonen, A. Smogunov, P. Umari, R. M. Wentzcovitch, QUANTUM ESPRESSO: a modular and open-source software project for quantum simulations of materials. *J. Phys. Condens. Matter* **21**, 395502 (2009).
80. P. Giannozzi, O. Andreussi, T. Brumme, O. Bunau, M. Buongiorno Nardelli, M. Calandra, R. Car, C. Cavazzoni, D. Ceresoli, M. Cococcioni, N. Colonna, I. Carnimeo, A. Dal Corso, S. de Gironcoli, P. Delugas, R. A. DiStasio Jr., A. Ferretti, A. Floris, G. Fratesi, G. Fugallo, R. Gebauer, U. Gerstmann, F. Giustino, T. Gorni, J. Jia, M. Kawamura, H. Y. Ko, A. Kokalj, E. Küçükbenli, M. Lazzeri, M. Marsili, N. Marzari, F. Mauri, N. L. Nguyen, H. V. Nguyen, A. Otero-de-la-Roza, L. Paulatto, S. Poncé, D. Rocca, R. Sabatini, B. Santra, M. Schlipf, A. P. Seitsonen, A. Smogunov, I. Timrov, T. Thonhauser, P. Umari, N. Vast, X. Wu, S. Baroni, Advanced capabilities for materials modelling with QUANTUM ESPRESSO. *J. Phys. Condens. Matter* **29**, 465901 (2017).

Acknowledgments

Funding: This work was supported by the National Research Foundation (NRF) of Korea Government (MSIT: NRF-2015R1A3A2031768, NRF-2020R1A2C3013454, NRF-2021R1A2C1008452, NRF-2021R1C1C1010660, NRF-2021R1A2C101116312, NRF-2022M3H4A1A04096465, and NRF-2023-RS-2023-00208825), the Republic of Korea's MSIT (Ministry of Science and ICT) under the ITRC (Information Technology Research Center) support program (IITP-2023-RS-2023-00259676) supervised by the IITP (Institute of Information and Communications Technology Planning & Evaluation), 2023 Research Fund (1.230022.01) of Ulsan National Institute of Science and Technology (UNIST), and Semiconductor R&D Support Project through the Gangwon Technopark (GWTP) funded by Gangwon Province (No. GWTP 2023-027). **Author contributions:** D.-S.K. conceived the original idea. H.Y.., G.J., and Jeeyoon Jeong fabricated the samples and performed the THz-TDS measurement and analysis. G.J., K.K., and H.-R.P. built the temperature-dependent THz-TDS setup. S.P. and Y.D.P. built the CPD setup, carried out measurements, and analyzed. H.A. and Joonwoo Jeong built the CA setup, carried out measurements, and analyzed. M.C. and N.P. performed the QM/MM calculations. H.-T.L. calculated the bulk indices from the experimental results and carried out the time-dependent heat transfer simulation. All authors analyzed the data and discussed the results. All authors wrote and approved the final draft of the study. H.-R.P., D.-S.K., and Jeeyoon Jeong supervised the project. **Competing interests:** The authors declare that they no competing interests. **Data and materials availability:** All data needed to evaluate the conclusions in the paper are present in the paper and/or the Supplementary Materials.

Submitted 3 November 2023
Accepted 21 March 2024
Published 24 April 2024
10.1126/sciadv.adm7315